Local and global numerical analysis of a porous screen in free-stream flow

by

Nicholas A. May-Varas

Submitted to the Department of Mechanical Engineering
in partial fulfillment of the requirements for the degree of
MASTER OF SCIENCE IN MECHANICAL ENGINEERING
at the
MASSACHUSETTS INSTITUTE OF TECHNOLOGY
May 2024

Authored by: Nicholas A. May-Varas
Department of Mechanical Engineering
May 30, 2024

Certified by: Wim M. van Rees
Associate Professor of Mechanical Engineering, Thesis Supervisor

Accepted by: Nicolas Hadjiconstantinou
Chairperson, Department Committee on Graduate Theses

Local and global numerical analysis of a porous screen in free-stream flow

by

Nicholas A. May-Varas

Submitted to the Department of Mechanical Engineering

on May 10, 2024 in partial fulfillment of the requirements for the degree of

MASTER OF SCIENCE IN MECHANICAL ENGINEERING

1 Abstract

A porous screen in a free-stream flow poses a model system for the analysis of nets, as used in fishing and aquaculture. In such applications, the forces on the net inform operational design and safety choices, whereas the flow past the net relates to the mixing of flow and nutrients in the wake. Most existing analyses of the flow past porous screens are based on experiments or simplified potential flow models. While both methods can lead to insightful results, open questions related to the details of the flow field, viscous effects, and the accuracy of the simplified models remain. To address these questions, we set up and run high-fidelity numerical simulations of the free-stream flow past a two-dimensional model porous screen. The screen is formed by placing a series of solid circular cylinders orthogonal to a free-stream flow. As the number of cylinders is increased, the gaps between them decreases, which increases the solidity of the screen. The use of a free-space domain removes any artificial numerical blockage effects, consistent with a free-stream flow.

Our analysis provides insights in the variation of the mean force coefficients as a function of the screen solidity, as well as their temporal fluctuations and spatial distributions across the screen. Further, we compute the flow rates and mean velocities through the screen gaps, and visualize the local flow field and wake. The results show that the mean value and fluctuations of the drag coefficients increase with the screen solidity. Further, the flow rate through the screen decreases monotonically as the solidity increases. The mean velocity through the screen behaves non-monotonically however, as it first increases and then decreases with screen solidity. Comparing our results to an existing potential model shows that the model predicts the flow rate well. However, the total drag coefficient is significantly lower in the predictions compared to the simulation results, pointing to the need for a better understanding of the pressure jump across the screen.

Thesis supervisor: Wim M. van Rees

Title: Associate Professor of Mechanical Engineering

Contents

1 Abstract **3**

2 Introduction **7**
2.1 Hydrodynamic Modeling of Net Dynamics 7
2.2 Panel Method 8
2.3 Potential Flow Method 10
2.4 Current Work 10

3 Methodology **11**
3.1 Numerical Methods 11
3.2 Simulation Setup 11

4 Results/Discussion **15**
4.1 Space-time and Temporal Averaged Forces and Flow Rates 15
4.1.1 Drag Coefficients 15
4.1.2 Flow Rate 16
4.2 Time-averaged Flow Rate For Each Gap and Time-averaged Forces For Each Cylinder 18
4.2.1 Local Flow Rate Analysis 18
4.2.2 Force Profiles 18
4.3 Time-averaged Velocity 20
4.3.1 Time-averaged Transverse Velocity Fields 20
4.3.2 Time-averaged Velocity Profiles 22
4.4 Space-time Averaged Flow Rate and Forces: Simulation and Potential Flow Analysis 24
4.4.1 Potential Flow Background Information 24
4.4.2 Flow Rate Comparison 25
4.4.3 Force Comparison 26

5 Conclusion/Future Work **27**

2 Introduction

Oceans are dynamic environments that present challenges for any structure operating in them. Changing currents, waves, and extreme weather events lead to everchanging forces on objects from ships and piers to porous screens, such as nets. Understanding the interaction between the flow and the objects is crucial to ensuring safety and preventing damage. The analysis of porous screens, such as nets, is a topic of continual interest. Understanding net hydrodynamics is crucial to ensuring the flow rate is sufficient to maintain a high water quality and to ensuring the net does not break. Figure 1 is a diagram of one aquaculture system [1].

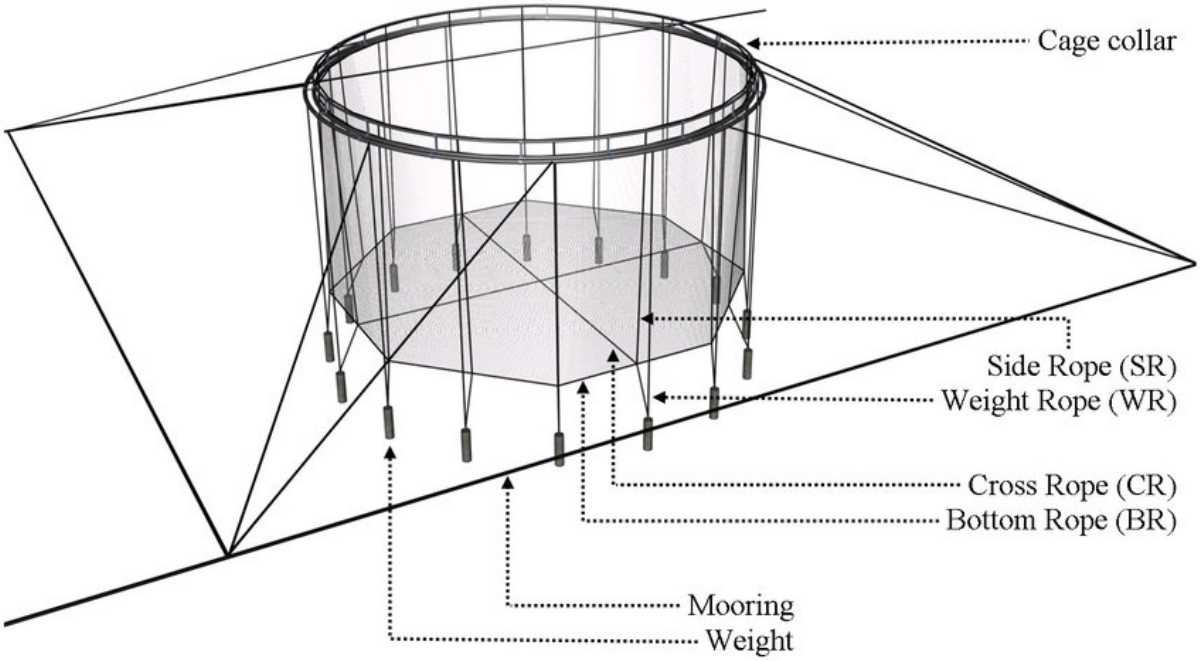

Figure 1: Diagram of an aquaculture system [1]

2.1 Hydrodynamic Modeling of Net Dynamics

Using hydrodynamic modeling techniques is a common method to gain a detailed understanding of the forces on and flow past nets. The hydrodynamic forces on a net contribute to the stresses on mooring lines and floats connected to the net and the net's volume change. Placing aquaculture nets in open-ocean environments has become a common trend with the goal of improving the water quality, however this also subjects the nets to harsher conditions[2]. We must incorporate the harsher conditions into our analyses to improve the durability of aquaculture systems. Environmental loads can account for most of the force on an aquaculture net [3][4], so we must develop accurate hydrodynamic models to capture all the forces on nets. The force information from the models helps us decide the materials and dimensions of an aquaculture system.

We must also analyze the movement of the flow past the nets because of its local and global effects. Bi et al. discusses the importance of studying the flow field because of its effect on the amount of dissolved oxygen and nutrient distribution [5]. The amount of dissolved oxygen and nutrient distribution can have a direct effect on the health of aquatic

life. The nets also reduce the flow downstream of the nets, which can have significant implications if aquaculture systems are placed downstream of other aquaculture systems.

There are a variety of methods to analyze flow past nets. Besides conducting model-scale and prototype-scale experiments, one can model flow past nets using numerical techniques. These methods can range from applying panel methods, potential flow methods, and methods that only use computational fluid dynamics (CFD).

2.2 Panel Method

The overall idea of the panel method is to calculate the force on discrete panels (which can include nodes and mesh bars) and then calculate total forces by summing all the forces. The method of calculating forces (called the Morison method) originated from the work by Morison et al., in which they derived an equation for the force on a cylindrical object [6]. The forces on the cylindrical object are drag and added mass force. While this method allows one to determine discrete forces, it is only applicable for analysing isolated cylindrical objects [6].

Tsukrov et al. [7] applied a finite element approach to modeling net panels. This method consisted of applying a modified Morison equation and consistent net elements to model a net. Furthermore, this method considers fluid drag and inertia forces, buoyancy, weight, mass inertia, and elastic forces, and the force coefficients are based on geometric parameters, Reynolds number, and relative fluid velocity. The model does not account for interactions between fluid flow in different regions of the domain, which can lead to inaccurate applied force results. The effect other strands have on the flow moving around a particular strand was accounted for by applying 'shadowing' coefficients in the analysis. This 'shadowing' effect accounts for local fluid flow interactions that are dependent on neighboring strands, which differs from the shielding effect that accounts for the total effect of the net on the velocity field. Modeling other components of an aquaculture net, such as the floating collar, are also important to include in a numerical analysis. Huang et al. [8] applied a lumped-mass method to model net dynamics of a net with a floating collar, and they also applied a modified Morison equation. Each panel consisted of four nodes and forces on each panel were evenly distributed to each node. The velocity reduction coefficient across the net (ratio of the downstream and free-stream velocity) was assumed to be 0.85. The even force distribution on each panel and the imposed velocity reduction coefficient do not fully account for the effects local fluid flow has on the entire velocity field and force distribution. Li et al. [9] improved the use of the lumped-mass model by implementing a mesh grouping method to reduce the number of meshes, and thus reduce the computational cost. The mesh grouping method combines meshes, while maintaining the same physical characteristics. They also set the drag and added mass coefficient of each point mass to be independent of motion direction. This method would not account for the time-dependent flow patterns that lead to varying drag and mass coefficients. The analysis conducted by Li et al. did not significantly focus on force distributions, which are important to consider when determining materials and anchoring systems to use. Therefore, Moe et al. [10] applied finite element analysis using a commercial FEA software to analyze a net. To reduce the computational cost, truss elements representing multiple twines were used. Similarly to the constant velocity reduction factor used by Huang et al. [8], they assumed velocity reduction percentages. This was found to not be a very accurate representation of the shadow (shielding) effect.

Rather than using velocity reduction percentages, Bi et al. [11] used a porous-media

model to simulate the flow around an entire screen. The porous-media model consists of using a pressure gradient equation and coefficients based on experimental results. For the porous-media model, the drag coefficient is a function of the solidity ratio and Reynolds number, while the lift coefficient is a function of solidity ratio and the attack angle. A lumped-mass model was used to model the motion of a flexible net. For the lumped-mass model, the drag coefficient equation on a mesh bar in the local normal direction was determined based on the Reynolds number. In this approach, there is only one equation for the drag coefficient equation on a mesh bar in the local tangential direction and that equation is a function of Reynolds number and the viscosity of water. Chen and Christensen [12] worked on reducing the computational time of the solver used in the research by Bi et al. [11]. They also used a porous-media and lumped-mass model. They reduced the simulation time by assuming a quasi steady-state condition for each time step. However, the drag force was consistently underestimated compared to experimental results.

Kristiansen and Faltinsen [13] used a modified screen model, instead of a Morison method, to model hydrodynamics forces on a net. A reason that the Morison method may not always be the most applicable option is because it can overestimate forces if the net's shape changes significantly [13]. The Morison method is a type of force model that calculates forces on individual twines of a net, while a screen model calculates forces (which are functions of solidity and inflow angle) on panels. The modified screen model was also a function of Reynolds number and included a wide range of solidity values. They derived an equation for a normal force coefficient by modifying a curve fit [14] that was based on experimental data [15]. The resulting expression (which was only applicable for solidity ratio less than or equal to about 0.5) was a function of the drag coefficient, solidity ratio, and the inflow angle. Drag and lift coefficients equations that were also a function of inflow angle were determined by using a Fourier series. They also applied a velocity reduction factor that was a function of an angle-independent drag coefficient and the solidity ratio. Yao et al. [16] applied a mass-spring model to simulate a net cage. They used a finite volume method the coupled the net and fluid. They also incorporated a hybrid volume methodology to couple the net and the flow field into the numerical framework. The drag and lift coefficients on each three-node panel were based on the method by [13]. However, one modification is three, instead of two, harmonics were used to calculate the lift coefficient. To improve the inaccuracy of the Morison method when applied to nets that rotate relative to the free-stream flow direction and to nets that change shapes, Bore et al. [17] developed a modified Morison model. To account for the angle of the net relative to the free-stream flow direction axis, they used screen model force coefficients to determine Morison coefficients. The modified Morison model accounted for the shielding effect by using the same velocity reduction coefficient as mentioned in the paper by Kristiansen and Faltinsen [13].

Endresen et al. [18] applied a similar approach as other researchers by considering a model that uses net elements with nodes to simulate a net, however they derived both local and global velocity equations. To incorporate a wider range of velocity reduction factors in the model, they used expressions based on Blevins virtual origin formula [19, 20]. One can use the formula to calculate a transverse velocity component downstream of a 2D circular cylinder. An assumption made in their work was that the contributions from each twine can be added, which contributed to the derivation of an equation to calculate an equivalent incoming velocity for each cylinder. The method led to the derivation of local and global velocity equations to model flow past an array of cylinders.

2.3 Potential Flow Method

The overall idea of the potential flow method is to model flow past a porous screen as potential flow, either by representing a porous screen as an array of potential flow sources or by just assuming potential flow through each gap. Equations for the flow rate and force are calculated as space-time averaged values over the entire array [21]. While this method does account for the screen affecting the entire flow field, typically forces are computed for the whole screen rather than individual net elements.

Taylor [22] analyzed flow past a screen consisting of point sources. The amount of flow that goes around the screen depended on the strength of the point sources. W.D. Baines and E.G. Peterson [23] analyzed flow past a screen across an entire channel, thus no flow is travelling around the outside edges of the screen. They used conservation methods to derive the equations for modeling the flow, assuming that potential flow occurs before and directly after the screen. They found that the flow would become unstable downstream of screens with high solidity ratios (greater than 0.5). This could contribute to larger deviations between theoretical and experimental results. Koo and James [24] improved upon previous research by deriving a mathematical model that was accurate for pressure drop coefficients up to 10 and could be generalized. For example, one could modify the method to analyze screens with non-uniform solidity and upstream velocity distributions. Steiros and Hultmark [25] used a similar approach, as they modeled a porous screen as a line of potential sources and then applied conservation of mass, momentum, and energy to derive equations for the screen's drag coefficient. One of the additions to the method was the incorporation of base suction and one of the assumptions was that no mixing occurs within a region directly downstream of the screen. Their results indicated better similarity with experimental results for higher solidity cases. We will further discuss their work in the methodology section because we compare our results with their results.

2.4 Current Work

The various studies summarized above apply methods to model flow past porous screens. However, there are disadvantages of using the panel and potential flow methods. A lack of a complete coupled flow field is one of the main reasons. The panel method is not always able to capture global flow effects, while the potential flow method is not always able to capture localized flow parameters. Further, both models rely on simplified drag force and pressure jump expressions that might limit their predictive ability.

Three-dimensional (3D) CFD simulations would lead to a very accurate representation of flow past a 3D net, however running 3D CFD simulations is computationally expensive. This motivates us to determine ways to reduce the computational cost, while still obtaining fundamental information. One method to realizing this objective is by first running 2D CFD simulations. The results from the 2D CFD simulations provide insights into trends and relations of flow past a porous screen. Some key results from the simulations are time-averaged flow fields, information regarding the similarities and differences between simulation and potential flow results, and velocity, flow rate, and force distributions. We have also not found any papers that conduct full CFD simulations and study small and large-scale flow dynamics. These points motivate us to conduct a study of flow past porous screens using CFD simulations as the main method.

To the best of our knowledge, this work presents the first high-fidelity simulation of the free-stream flow past porous screens of various solidities. We consider the time-averaged global hydrodynamics of the screen by analyzing the total drag force on the screen and

the flow rate through the gaps. Further, we consider the flow rates through each gap to determine any local trends from the data. Following that discussion, we consider the drag and lift force on each cylinder in order to understand the distribution of the forces across the height of the screen. Moreover, we consider time-averaged velocity fields, time-averaged velocity profiles as a function of y-position, and a time-averaged velocity profile as a function of x-position. Finally, we compare our numerical results from flow rate, velocity, and drag force to predictions from the porous screen model [25].

3 Methodology

We apply a numerical approach to study flow past porous screens of varying solidities. The following sections describe the numerical solver, simulation domain and analysis parameters, and mesh convergence results.

3.1 Numerical Methods

We use a two-dimensional incompressible viscous Navier-Stokes solver based on the vorticity-velocity formulation, with an immersed interface method to discretize the boundaries [26, 27]. The vorticity-velocity formulation enables the use of free-space simulations in the top/bottom and inflow directions, reducing the need to have a large distance between the edge of an object and the edge of the domain. The implementation relies on a second-order finite-difference discretization of the differential operator and a Fast Fourier Transform with a Lattice Green's Function kernel for the velocity reconstruction. Full details of the algorithm and implementation are provided in [26].

3.2 Simulation Setup

The 2D domain and computational setup used in this work is sketched in Figure 2. We generate a uniform mesh with the number of cells per cylinder diameter equalling 75. The right side of the domain is an outflow boundary condition [26], while the left, top and bottom domain boundaries are free-space, so that the flow is free to enter or exit along these boundaries. The domain size and position of the porous screen are chosen to maintain the vortical wake within the domain. The distance from the top/bottom edge of every porous screen to the edge of the top/bottom domain boundary is 15 diameters. Also, the distance from the right edge of every porous screen to the outflow boundary is 30 diameters, consistent with a study on the outflow domain boundary location in [26]. The distance from the left edge of every porous screen to the inflow boundary is 4.5 diameters.

A free-stream velocity U_∞ is applied according to a Reynolds number of $Re = U_\infty D/\nu = 150$, based on a single cylinder diameter D and fluid viscosity ν. The height of the porous screen in all simulations is equal to $H = 10D$. We analyze a variety of solidity values $S = ND/H$, with $2 \leq N \leq 7$ being the number of cylinders distributed equally across the screen. The solidity then gives $0.2 \leq S \leq 0.7$, which is within a similar range to the values considered in other studies.

Due to the unsteady flow, we decide to run each of the simulations for 500 convective time units (time normalized by the free-stream velocity and cylinder diameter). In order to induce vortex shedding in the simulation, and thus reduce the overall simulation time, we break symmetry by adding a velocity perturbation in the y-direction at the beginning of the simulation. Specifically, the perturbation is implemented gradually, starting from

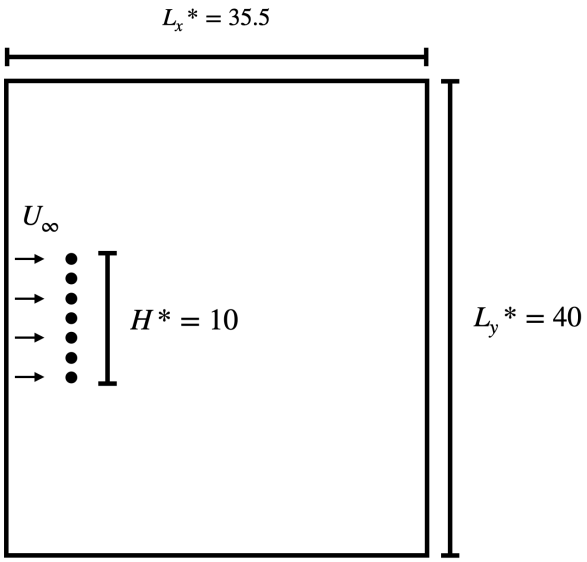

Figure 2: Diagram of the domain used for all of the simulations

$t = 3.75$ and then reaching a vertical velocity value of $v/U_\infty = 1$ at $t = 7.5$, and then gradually reducing back to zero until $t = 11.25$.

Throughout this paper, we use a consistent set of variables (unless otherwise specified) to denote normalized velocities, flow rates, and force coefficients. We normalize position by cylinder diameter D, velocity by free-stream velocity U_∞, and time by the convective unit U_∞/D. An asterisk above transverse and vertical velocity values (u and v) denotes a space-averaged value over all gaps (u^* and v^*), while an asterisk above flow rate values (q) denotes a summation of flow rates over all gaps (q^*). An asterisk for forces denotes a summation over all cylinders (N is the number of cylinders) (C_D^* and C_L^*). Also, a variable with just an overbar denotes a time-averaged velocity value, flow rate through one gap, or force coefficient for one cylinder. The values are time-averaged over about 300 time units ($\overline{u}, \overline{q}, \overline{C_D}, \overline{C_L}$). Flow rates are normalized by $U_\infty H$ and forces are normalized by $\frac{1}{2}\rho U_\infty^2 H$, where H is the height of the porous screen. Solidity is defined as $S = \frac{ND}{H}$ (Porosity $\equiv \beta = 1 - S$).

To find an appropriate numerical resolution for our simulations, we conduct a convergence study. We run simulations with the highest solidity porous screen ($S = 0.7$) with mesh resolutions ranging from 25 to 150 grid points/diameter and calculate the flow rates through each gap (q). Figure 3 shows the flow rate results over time for each of the six gaps, for all resolutions. The simulation time is less than for the simulations discussed later, so that the flow does not yet destabilize due to the interactions of the vortices in the wake. The results indicate that the flow rates are quite similar to each other. The time-averaged flow rate through all of the gaps for the case with a mesh resolution of 75 grid points/diameter is within 5% of the time-averaged flow rate for the case with a resolution of 150 grid points/diameter. The similarities are also evident based on the velocity profile shown in Figure 4, which is based on velocity data at a time of 13.2 time units (number of t values). Given that $S = 7$ is the most stringent case in terms of resolution requirements, we conclude that a mesh resolution of 75 grid points/diameter is reasonable to obtain accurate results for all simulations, while also ensuring a reasonable computational time.

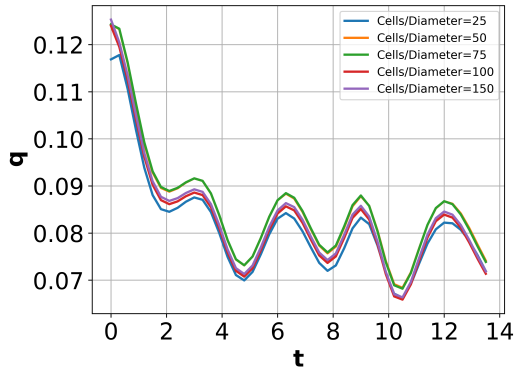

(a) Gap 1

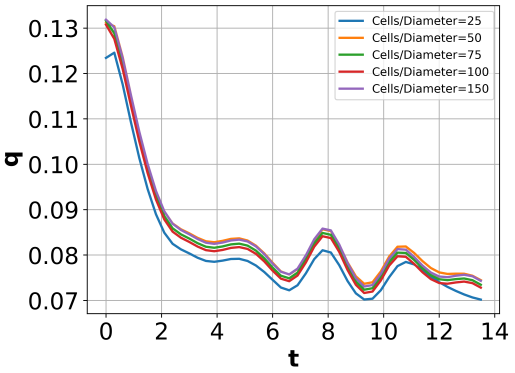

(b) Gap 2

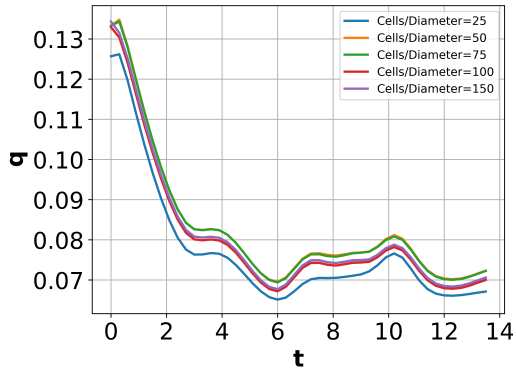

(c) Gap 3

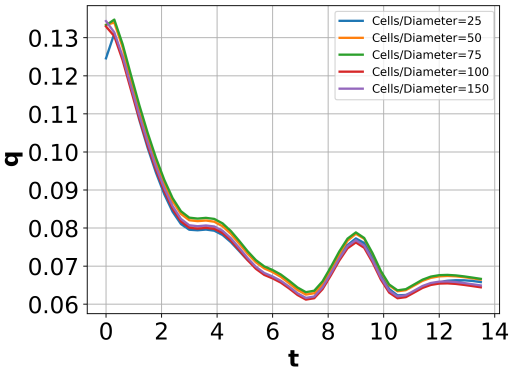

(d) Gap 4

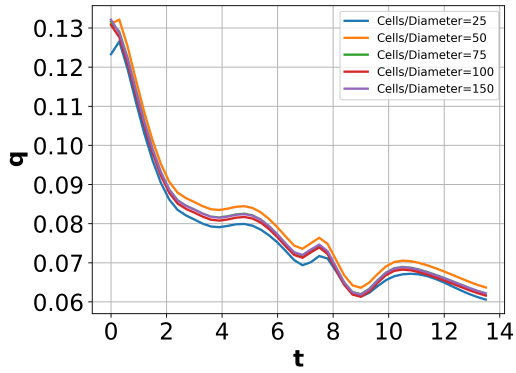

(e) Gap 5

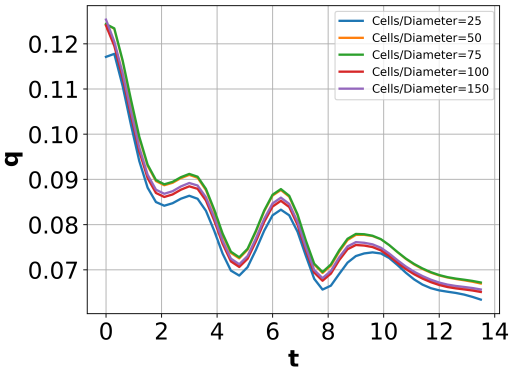

(f) Gap 6

Figure 3: Normalized normalized flow rate through each gap as a function of time and mesh resolution

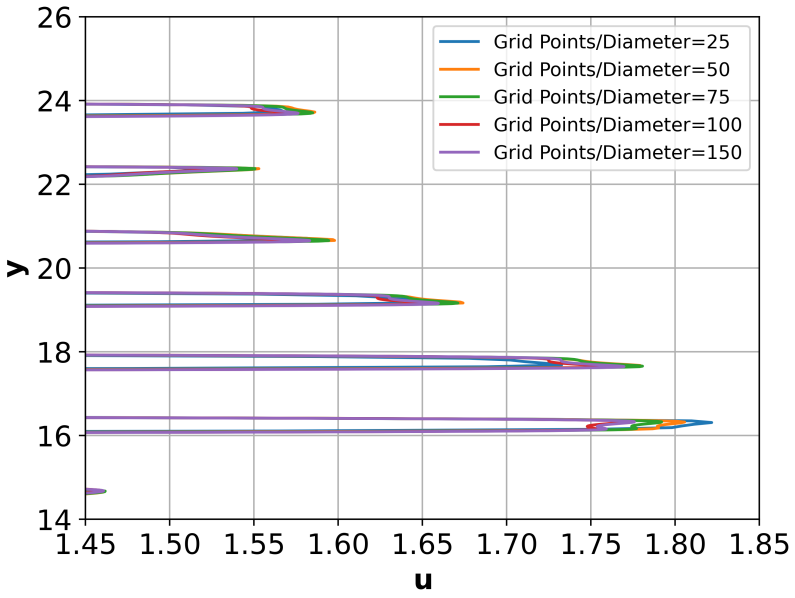

Figure 4: Velocity profiles at x=0.5 and t=13.2 for cases with different mesh resolutions

4 Results/Discussion

The following sections describe the variety of results from our analysis and work towards answering the questions we previously mentioned. The analyses are focused on understanding the local and global parameters of flow past porous screens in terms of velocity, flow rate, and force. We apply error bars to the simulation results, which are based on standard deviations of time-domain simulation results.

4.1 Space-time and Temporal Averaged Forces and Flow Rates

The following sections discuss time-averaged and temporal drag coefficient and flow rate results from simulations of porous screens (solidity values range from $S = 0.2$ to $S = 0.7$).

4.1.1 Drag Coefficients

Figure 5 shows the time-averaged drag coefficient on the entire porous screen for various cases. The results indicate that as solidity increases, the total force on the screen also increases. One cause of the significant difference between the $S = 0.2$ and $S = 0.7$ cases is that the drag coefficient is normalized by the height of the porous screen, and not projected area. However, this is not the only cause of the difference because when we normalized the drag coefficient by the projected area, the same trend still occurs, although there is less of a difference between drag values. Another reason for the trend is the shielding effect. The porous screen has a greater effect on the flow as the solidity increases. The temporal variations are also important to study because the forces at each point in time should be considered when designing a net. The results from all of the cases are shown in Figure 6 with the percent error between the sum of the drag coefficient for all cylinders and the average drag coefficient for all cylinders plotted as a function of time. One trend is that the range of values tends to increase as the solidity increases. This could be caused by increased mixing of shedded vortices when solidity increases.

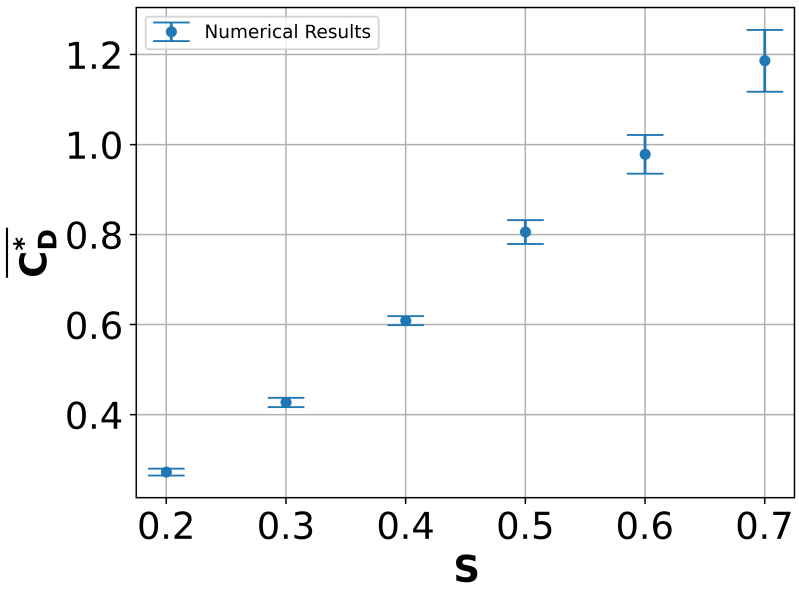

Figure 5: Total drag coefficients results from simulations as a function of the solidity

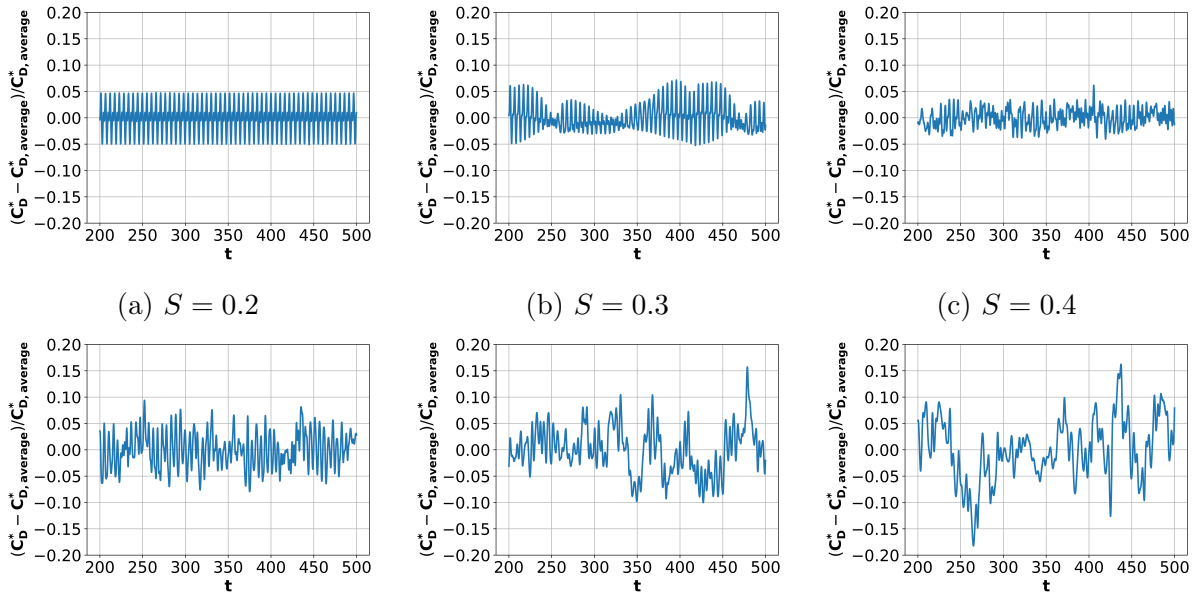

(a) $S = 0.2$ (b) $S = 0.3$ (c) $S = 0.4$

(d) $S = 0.5$ (e) $S = 0.6$ (f) $S = 0.7$

Figure 6: Sum of the drag coefficient for all cylinders on the porous screen for each case

4.1.2 Flow Rate

We now study the q^* values for all of the gaps in the porous screen. Regarding the time-averaged flow rates (Figure 7), we observe that the range of q^* values decreases non-linearly as a function of solidity. As the screen's solidity increases, it becomes more like a solid plate, so one would expect there is less flow going through the screen. Figure 8 shows the q^* time series for each case. One trend we observe is as the solidity increases, the flow rate results become less harmonic and more irregular, with larger amplitudes. This is due to the increased interaction between the flow past each cylinder. Vortices will shed from each cylinder almost periodically. For higher solidity cases, the vortices that are shed interact with each, which contributes to the flow rate not having a very periodic trend over time. In the case of the flow rate past a net, a more variable pattern over time could affect the durability of the net and the health of the life close to the net.

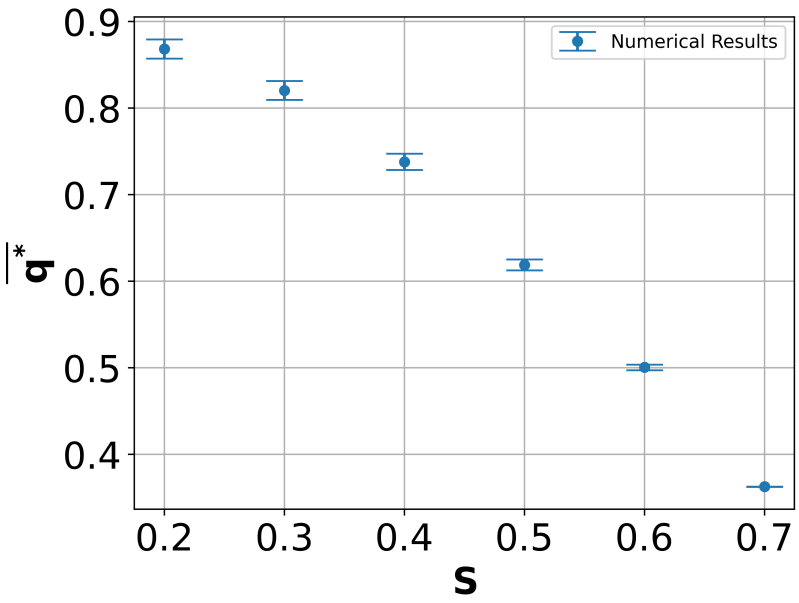

Figure 7: Total transverse flow rate results across the porous screen from simulations as a function of solidity

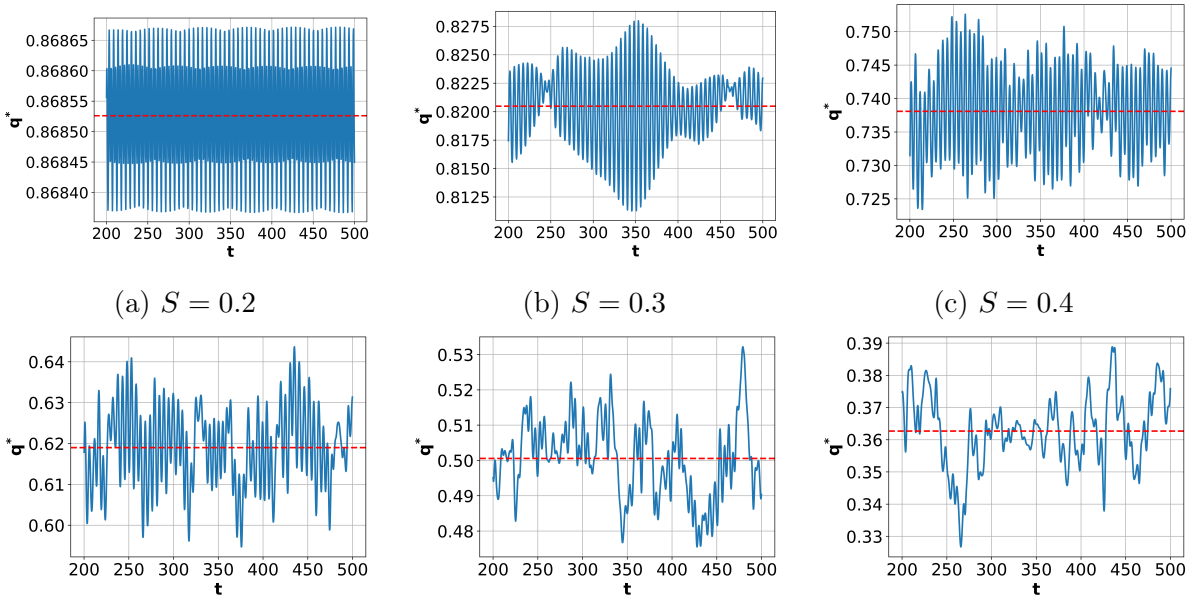

(a) $S = 0.2$ (b) $S = 0.3$ (c) $S = 0.4$

(d) $S = 0.5$ (e) $S = 0.6$ (f) $S = 0.7$

Figure 8: Total flow rate across the porous screen for each case. The dashed red line corresponds to the mean total flow rate through the screen.

4.2 Time-averaged Flow Rate For Each Gap and Time-averaged Forces For Each Cylinder

The following sections discuss results related to the time-averaged flow rate for each gap and the time-averaged drag and lift force for each cylinder.

4.2.1 Local Flow Rate Analysis

The fluid flow through each gap is another important parameter to study. To compare the flow rates among each other and compared to the flow rate if the flow was evenly distributed, we calculate the percent difference between the simulation flow rate to the evenly distributed flow rate as shown by the following equations.

$$\overline{q_{average}} = \frac{1}{N-1} \tag{1}$$

$$\%\text{Difference} = \frac{\overline{q} - \overline{q_{average}}}{\overline{q_{average}}} \tag{2}$$

Figure 9 shows the results from the analysis. For the lower solidity cases (< 0.5), the flow generally evenly distributes through each gap, with the maximum percent difference being about 0.5%. For the higher solidity cases (≥ 0.5) the differences between the normalized flow rates increases. For example, the absolute value of the difference between the maximum and minimum value for the $S = 0.4$ case is 0.008, while that value is 0.027 for the $S = 0.6$ case. This result shows that the flow becomes increasingly non-uniform across the screen as the solidity increases.

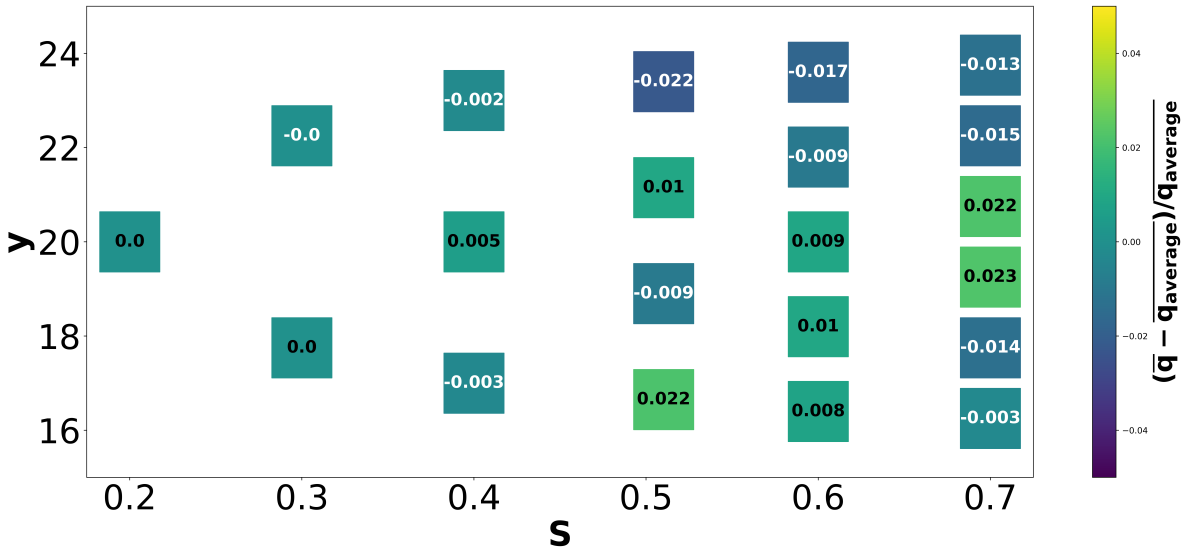

Figure 9: Comparison of the flow rate results compared to a normalized flow rate that is evenly distributed

4.2.2 Force Profiles

By examining the drag and lift coefficients as a function of cylinder and solidity, we gain insights into the force profile and relations between forces and velocities. Figure 10 shows

normalized drag coefficients for all of the cases. The normalized drag coefficients are obtained by calculating the percent difference between the drag coefficient on one cylinder and the average drag coefficient. This method is useful for analysing the force distribution on the screen with finite elements. We use the following equations to calculate the percent difference.

$$C_{D,average} = \frac{\sum_{i=1}^{N} \overline{C_D}}{N} \tag{3}$$

$$\%\text{Difference} = \frac{\overline{C_D} - \overline{C_{D,average}}}{\overline{C_{D,average}}} \tag{4}$$

One observation is the force distribution is less uniform for higher solidity porous screens. For example, the difference between the largest and smallest normalized drag coefficient for the $S = 0.2$ case is about 0, while the difference between the largest and smallest normalized drag coefficient for the $S = 0.7$ case is about 0.44. Another example is the minimum normalized drag coefficient for the $S = 0.6$ case is -19%, while that value is about zero for the $S = 0.2$ case. Another observation is the normalized drag coefficient for the center cylinder corresponding to the $S = 0.7$ is much larger than the normalized drag coefficients for the edge cylinders. This relates to the non-uniform flow rate through the gaps caused partially by the large solidity. The uneven force distribution is important to consider when designing a net system because one would want to ensure each node can withstand the applied loads.

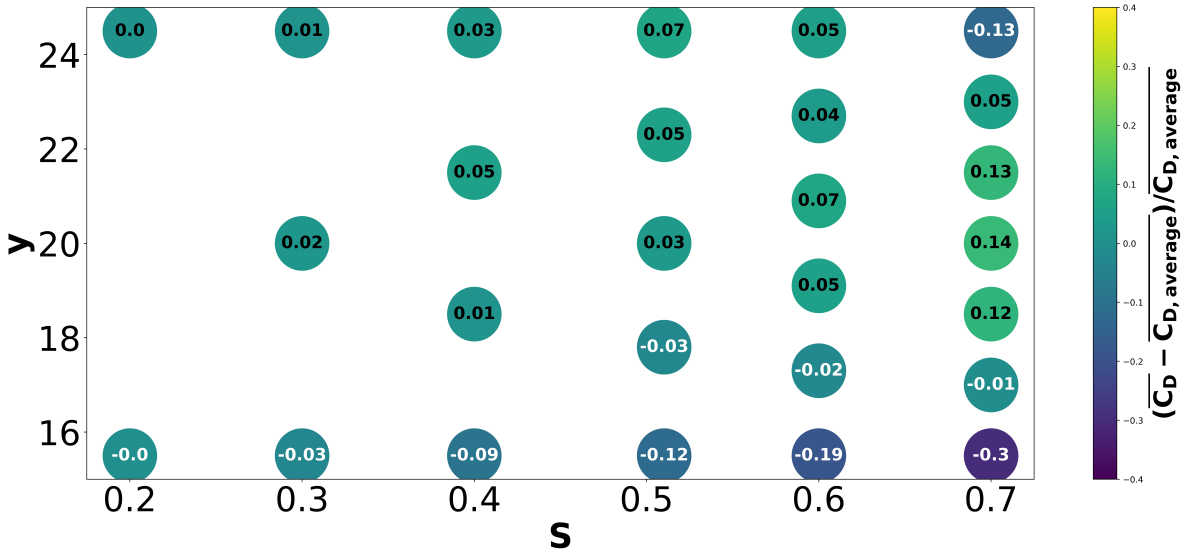

Figure 10: Comparison of the drag coefficient results compared to a drag coefficient that is evenly distributed

We also consider the lift coefficient using a similar methodology. However, one difference in our analysis is that we normalize the lift coefficient for each cylinder by the sum of the absolute values of the lift coefficients on all the cylinders (Equation 5). The resulting value informs us of how much lift force is applied on a cylinder compared to the total lift force on the porous screen.

$$\overline{C_L*} = \frac{\overline{C_L}}{\sum_{i=1}^{N} |\overline{C_L}|} \tag{5}$$

One observation we make from Figure 11 is the symmetry of the lift coefficients across the centerline ($y = 20$). For example, the magnitudes of the normalized lift coefficients for the $S = 0.2$ case only differ by about 0.04, and the magnitudes of the outer two cylinders for the $S = 0.6$ case only differ by about 0.01. Another symmetry observation is that the sign of the lift coefficients is flipped across the centerline. This indicates a repulsive force between the cylinders above the centerline and the cylinders below the centerline. This repulsive force would have significant implications if the cylinders were not fixed in space, but rather connected by "springs". When designing a porous screen, one would want to consider the material used to account for repulsive forces, as indicated by our results. We also observe that the absolute value of the normalized lift coefficient for each cylinder tends to increase as the y of the cylinder increases. A main cause of increasing and decreasing lift forces is likely due to the flow rate through each gap not being uniform. Another possible cause is the non-uniform vertical velocity upstream of the screen. The vertical velocity profile at $x = 4.0$ for the $S = 0.7$ case is shown in Figure 12. The absolute value of the time-averaged vertical velocity tends to increase farther from the center of the screen. This likely contributes to the larger lift force for the cylinders farther from the center.

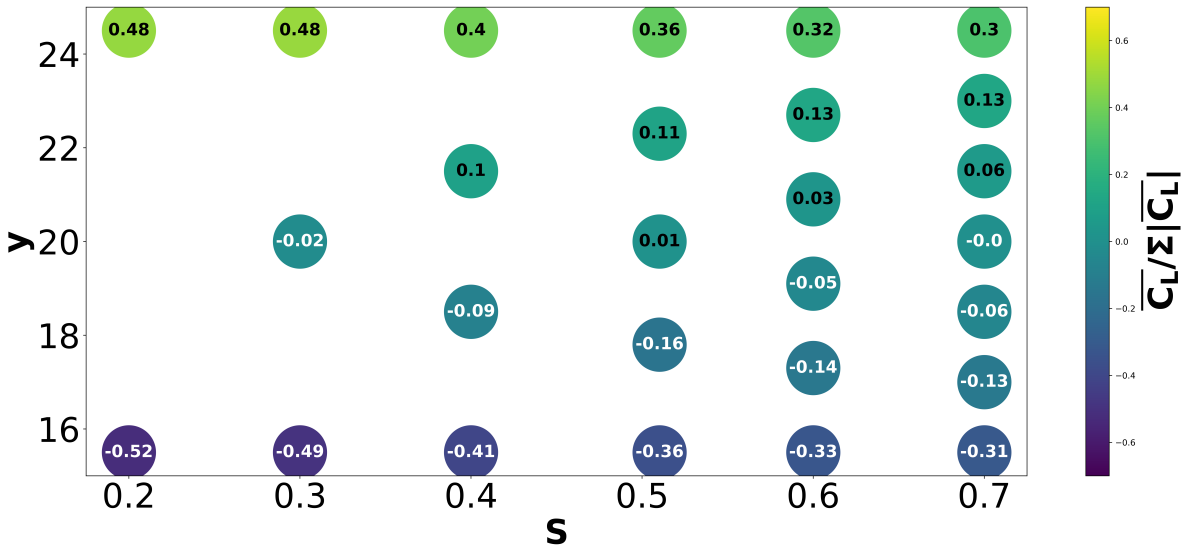

Figure 11: Normalized lift coefficient results for all of the cases

4.3 Time-averaged Velocity

The following sections discuss results related to time-averaged transverse velocity fields and time-averaged velocity profiles.

4.3.1 Time-averaged Transverse Velocity Fields

We first study the time-averaged transverse velocity field from each of the simulations. The time-averaged flow fields shown in Figure 13 indicate multiple patterns. One observation

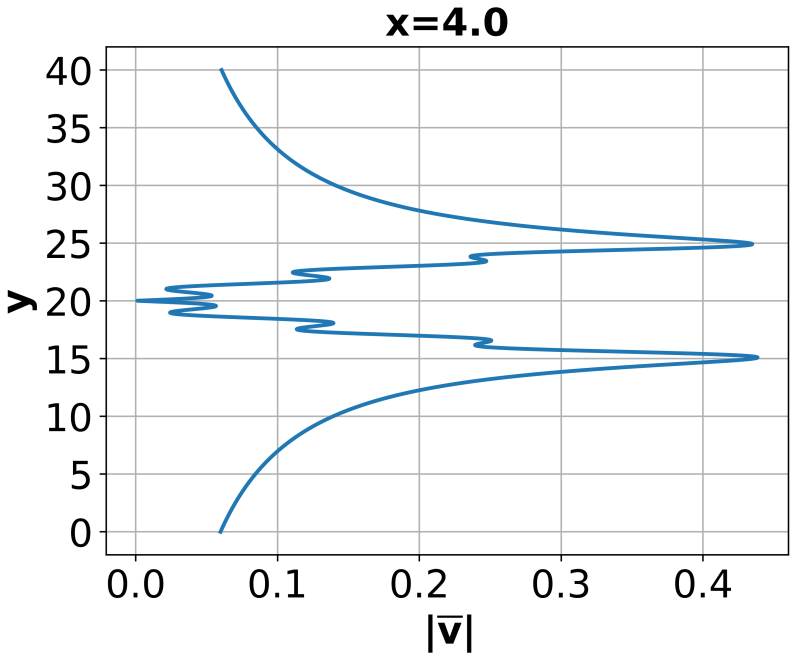

Figure 12: Vertical velocity profile at $x = 4.0$ for the $S = 0.7$ case, which is 0.5 diameters upstream of the screen

is that higher solidity porous screens have a greater effect on the velocity values compared to the lower solidity porous screens. This decrease in $\overline{u}$ as solidity increases is related to the idea of the shielding effect. If one considers the solidity limits, as the solidity goes to one (a non-porous screen), the $\overline{u}$ of the fluid directly downstream of the non-porous screen would likely trend towards zero. As the solidity goes to zero (no porous screen), the $\overline{u}$ value does not change in the entire domain. In the case of an aquaculture net, the shielding effect can have significant implications. One of the goals of the aquaculture net is to ensure that there is a significant amount of flow across the net in order to ensure the water inside the net does not contain a high level of toxins. Based on this, and the shielding effect results shown in Figure 13, one should ensure the solidity of the net is not too large as to increase the concentration of toxins. Another observation is the increased width of the wake as the solidity increases. The wake width in the plots shown in Figure 13 is approximately the height of the blue region. The wake width is important to consider because it informs us of how large of a region the porous screen is affecting. For example, if one placed multiple aquaculture nets in an array, they should consider the spacing of the nets. The results indicate that nets placed offset from each other (even if they are not right behind each other) can affect the dynamics of the other net. Thus, one must consider the effects that the additional nets have on each other, rather than only considering isolated nets in analyses. Another interesting observation is directly behind the screen, the velocity tends to be smallest behind the edge cylinders compared to the velocity behind the center cylinders. However, far downstream, the velocity tends to be smallest behind the center cylinders compared to the velocity behind the edge cylinders.

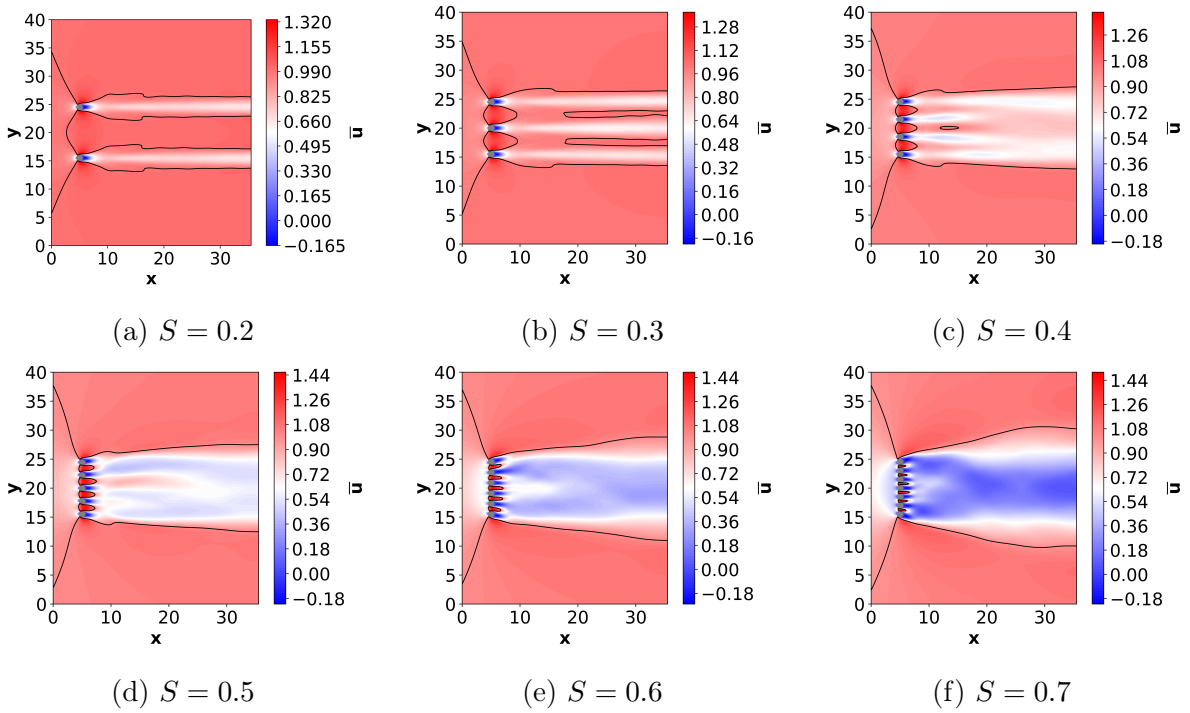

(a) $S = 0.2$ (b) $S = 0.3$ (c) $S = 0.4$

(d) $S = 0.5$ (e) $S = 0.6$ (f) $S = 0.7$

Figure 13: Time-averaged transverse velocity fields for each case with the black contour lines indicating $\overline{u} = 1$

4.3.2 Time-averaged Velocity Profiles

Since one of the goals of this work is to gain a more detailed understanding of the flow past porous screens, we examine time-averaged velocity and force profiles. This localized velocity and force analysis allows us to understand how the flow is affected in different regions of the screen and how the force profile is related to the localised flow dynamics.

We first analyze the velocity profiles as a function of y at various x locations (x=4.5, 5.0, 5.5, and 6.0) with the goal of understanding how the porous screen affects the fluid flow. Figure 14 demonstrates the shielding affect and local fluid acceleration caused by the porous screen. As the fluid approaches the screen, it slows down and some of the flow travels around the screen and some eventually accelerates through the gaps due to the conservation of mass. As evident in the x=5.0 plot (in the center of the porous screen), the flow is travelling faster closer to the cylinders and relativity slower farther from the cylinders.

To complement these velocity profiles we study the velocity profiles as a function of x and the y location equal to the center of the computational domain (y=20). Figure 15 is another way of demonstrating the fluid flow characteristics passing the porous screen at $x \approx 5.0$. Regarding the cases with an even number of cylinders (there is no cylinder at this y-value), as the solidity increases, the $\overline{u}$ value at $x \approx 5.0$ also increases. In contrast, upstream of the cylinders, as S increases, $\overline{u}$ decreases. The increase in velocity through the gap is due to conservation of mass and the decrease in velocity before the screen is due to the shielding effect. Another observation is that far downstream of the porous screen (about 30 diameters), the $\overline{u}$ from the $S = 0.2$ case is the only value that returns to the free-stream velocity, while all the other values are less than the free-stream velocity. The $\overline{u}$ values far downstream decrease as the solidity increases. This is related to the shielding effect discussion regarding the time-averaged $\overline{u}$ field. To reiterate, as the solidity increases,

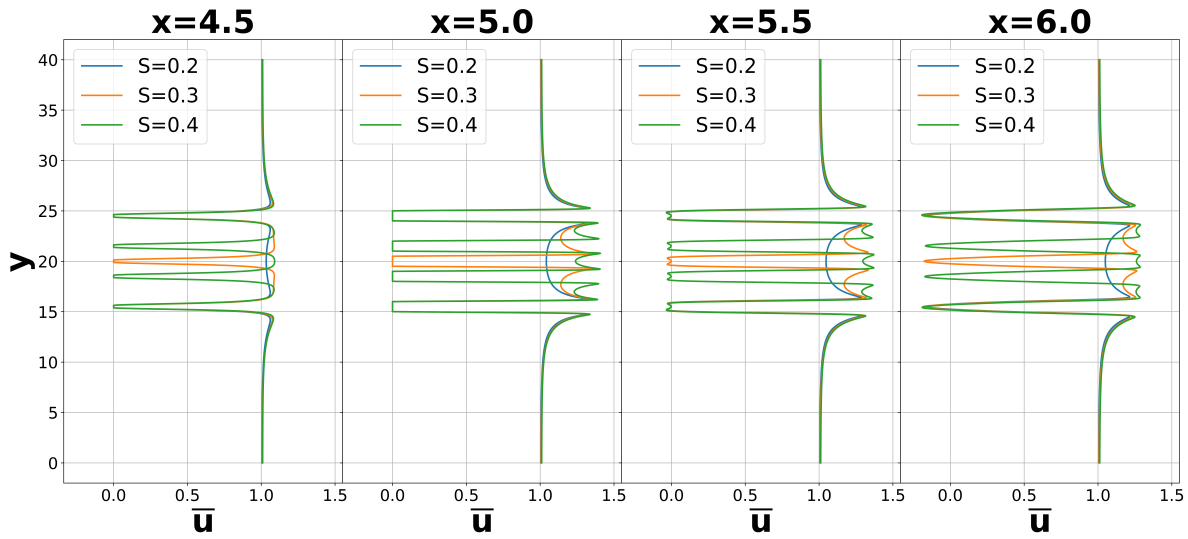

Figure 14: Transverse velocity profiles for at multiple x locations and for three of the cases

the porous screen has a greater effect on the flow, which in this example is evident by the significant decrease in $\overline{u}$ about 30 diameters from the porous screen. This decrease in velocity could have positive or negative effects depending on the specific application of the porous screen. In the case of an aquaculture net, the velocity should not reduce too much because that would reduce the safety of the local water. For other applications, such as breakwaters, the reduction in velocity far downstream of the breakwaters is advantageous.

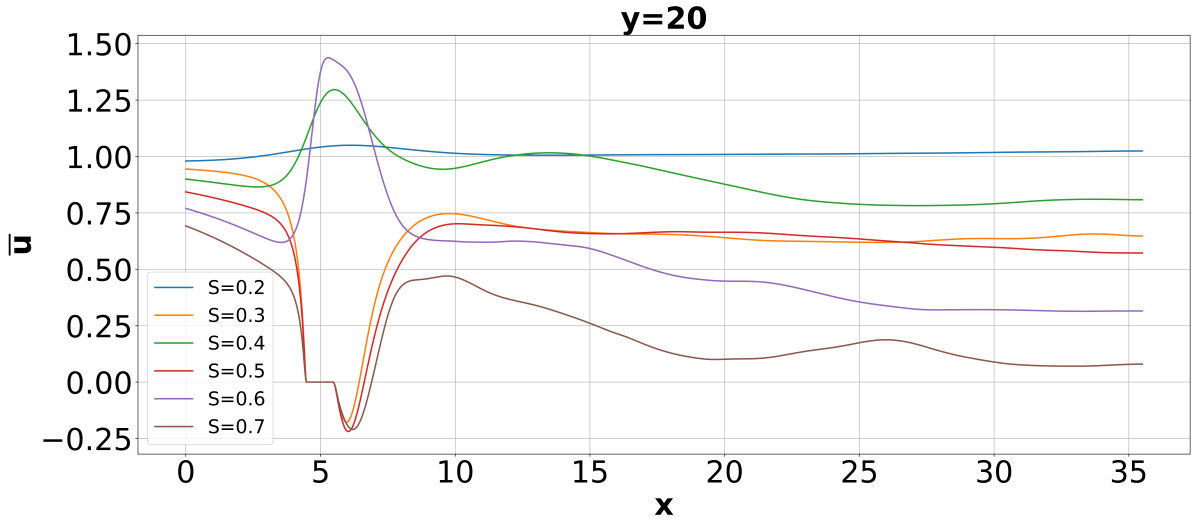

Figure 15: Transverse velocity profiles along the centerline ($y = 20$) and for all of the cases

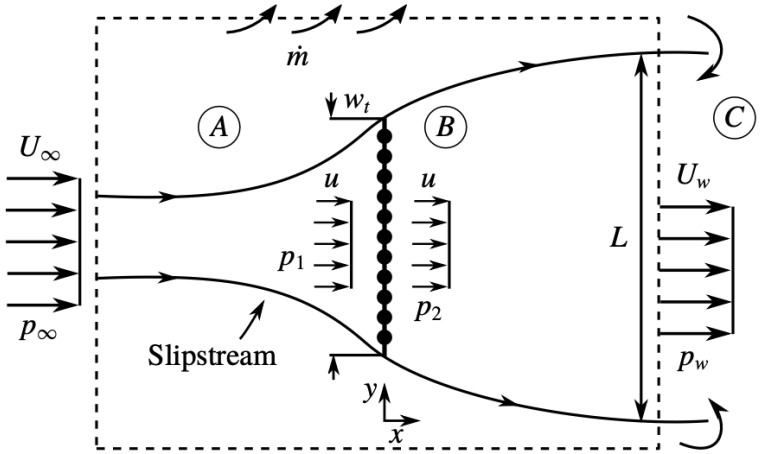

Figure 16: Diagram of the domain used in the work by Steiros and Hultmark [25]

4.4 Space-time Averaged Flow Rate and Forces: Simulation and Potential Flow Analysis

As described in the Literature Review section, many researchers have developed methodologies to simulate flow past porous screens. In the following section we compare our flow rate and force results with those obtained from a potential flow analysis. We consider equations mentioned in the paper by Steiros and Hultmark [25], who applied potential flow results from [22][24] with the addition of base suction. The information in the next section provides an overview of the potential flow equations we consider.

4.4.1 Potential Flow Background Information

An overview of domain is shown in Figure 16, which is included from the paper by Steiros and Hultmark [25]. The flow is region A is modeled by Taylor's model [28]. This means the flow in region A can be modeled using a potential flow approach. The potential flow solution is based on representing the screen as an array of potential sources having a strength m. The flow in region B is also assumed to be inviscid and irrotational, however the velocity is scaled down due to mass conservation. Another condition of the model is that there is no flow mixing between region A and B. Mixing and viscous effects are only applied in region C, which leads to a 'base-suction' effect. To account for conservation of mass while still using a potential flow solution for regions A and B, a velocity reduction factor (Eq. 6) is used to calculate the wake velocity ($U_w = U_\infty E$).

$$E = \frac{U_\infty - \frac{m}{2}}{U_\infty + \frac{m}{2}} = \frac{\overline{q^*}}{2 - \overline{q^*}} \tag{6}$$

Drag coefficient equations are derived by applying conservation of mass, momentum, and energy. Equation 7 is the result of a momentum balance accounting for base suction.

$$\overline{C_D^*} = \frac{4}{3}\frac{(1 - \overline{q^*})(2 + \overline{q^*})}{(2 - \overline{q^*})} \tag{7}$$

A drag coefficient that incorporates the solidity of the screen is derived by considering the pressure jump across the screen. With the assumption of inviscid flow, equations 8 and 9

are combined to obtain equation 10. Combining these two equations leads to an equation for $\overline{q^*}$ as a function of S and an equation for $\overline{C_D^*}$ as a function of S.

$$p_h = p_1 + \frac{1}{2}\rho\overline{q^*}^2\left(1 - \frac{1}{(1-S)^2}\right) + \frac{1}{2}\rho\overline{q_v^*}^2 \tag{8}$$

$$p_2 + \frac{1}{2}\rho\overline{q^*}^2 + \frac{1}{2}\rho\overline{q_{v,w}^*}^2 = p_h + \frac{1}{2}\rho\overline{q^*}^2 \tag{9}$$

$$\overline{C_D^*} = \overline{q^*}^2\left(\frac{1}{(1-S)^2} - 1\right) - \frac{4}{3}\frac{(1-\overline{q^*})^3}{(2-\overline{q^*})^2} \tag{10}$$

4.4.2 Flow Rate Comparison

Figure 17a shows the simulation and potential flow results of the flow rate across an entire porous screen. We obtain the flow rate equation by combining equations 12 and 13 from the work by [25].

The simulation and potential flow results both indicate that the flow rate increases as the solidity decreases, which is consistent with the time-averaged velocity field results in the downstream direction of the screens. We also observe that the maximum percent difference between the potential flow and simulation results occurs for a solidity of 0.4 with the percent difference being less than 7%. The shape of the potential flow results and simulation results are also similar. However, for solidity values between 0.2 and 0.7, all of the simulation results are larger than the potential flow results, which indicates less flow is moving around the porous screen in the simulation compared the porous screen applied by Steiros and Hultmark [25]. A possible cause of the numerical differences could be the assumption of no mixing occurring in region B (shown in Figure 16. The vortex shedding and inherent mixing that occurs would affect the flow rate, and therefore should be included in the analyses.

Since $\overline{u^*}$ is directly related to $\overline{q^*}$ ($\overline{u^*} = \frac{\overline{q^*}}{(1-S)}$) , we also consider the relation between $\overline{u^*}$ and S. The results shown in Figure 17b indicate that $\overline{u^*}$ increases until $S = 0.5$ and after that point, $\overline{u^*}$ decreases. The solidity value of 0.5 was also noted in the work by Baines and E.G. Peterson [23]. They discussed that for solidity values greater the 0.5, the flow downstream of the screens becomes unstable. Regarding our results, we hypothesize that as the solidity increases from 0.2 to 0.5, the shielding effect is not significantly affecting the flow. However, for solidity values greater than 0.5, the shielding effect becomes prominent and causes the velocity to start decreasing through the gaps.

We also compare flow rate in the transverse direction from the simulations to the transverse flow calculated using the following equation [25] [22].

$$\overline{v^*}^2 = \frac{(1-\overline{q^*})^2}{3} \tag{11}$$

As previously referred to, as the solidity decreases, the $\overline{q^*}$ increases. Thus, the results shown in Figure 18 indicate that the flow rate in the transverse direction decreases as $\overline{q^*}$ increases. This trend is consistent with the shielding effect. As the flow rate through the gaps increases, the flow is deflected less by the presence of the screen, causing the flow rate in the transverse direction to decrease. We also consider the differences between the potential flow and simulation results. The largest percent difference between the potential flow and simulation results is about 40%, which occurs for a $\overline{q^*}$ of about 0.35.

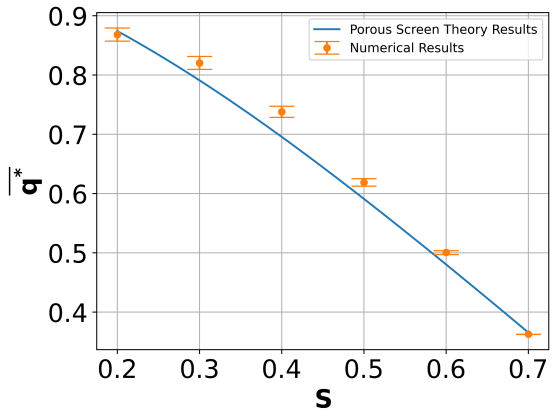

(a) Total transverse flow rate results across the porous screen from simulations and potential flow theory as a function of solidity

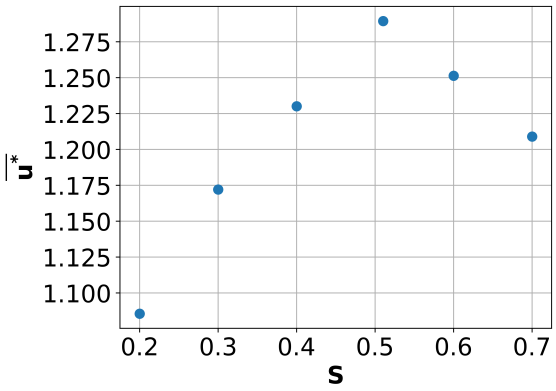

(b) Space-time averaged transverse velocity simulation results for all cases as a function of solidity

Figure 17

This is a significant difference that could be caused by multiple factors. One reason for the significant differences would be the location in which the $\overline{v^*}^2$ values are obtained. We use the $\overline{v^*}^2$ values that are 0.5 diameters upstream of the cylinders, instead of calculating $\overline{v^*}^2$ based on the horizontal flow rate.

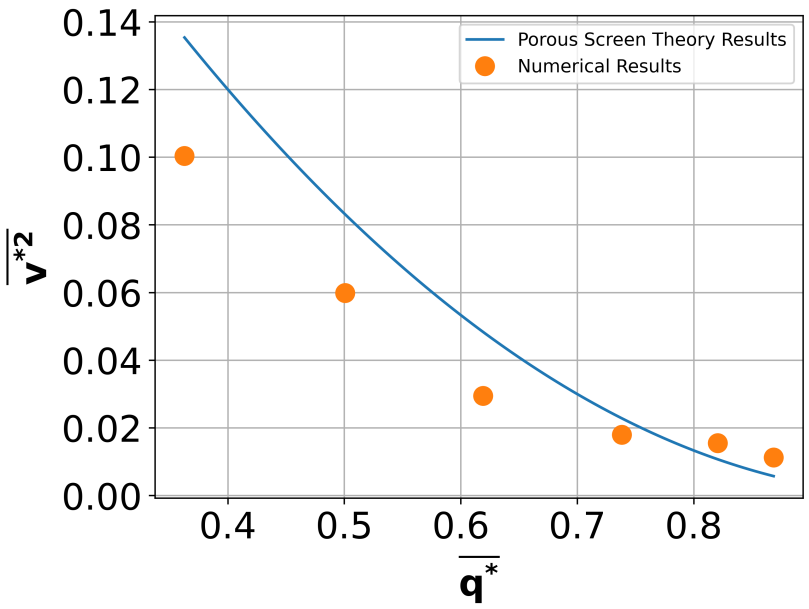

Figure 18: Total vertical flow rate results across the porous screen from simulations and an equation as a function of the total flow rate

4.4.3 Force Comparison

We consider the drag coefficient on the porous screen based on simulation results (normalized by the height of the porous screen) and by using equations from the paper by

Steiros and Hultmark [25]. We use Eq. 12 (shown below for reference) to obtain the drag coefficient and the flow rate (q) is obtained by combining equations 12 and 13.

$$\overline{C_D^*} = \frac{4}{3}\frac{(1-\overline{q^*})(2+\overline{q^*})}{(2-\overline{q^*})} \tag{12}$$

$$\overline{C_D^2} = \overline{q^*}^2\left(\frac{1}{(1-S)^2}-1\right) - \frac{4}{3}\frac{(1-\overline{q^*})^3}{(2-\overline{q^*})^2} \tag{13}$$

Figure 19a shows the simulation and potential flow results of the total drag coefficient on the porous screen for various solidity values. The simulation results differ significantly from the potential flow results with the largest percent difference being about 50%, which corresponds to a solidity of 0.4. We also consider the $\overline{C_D^*}$ vs. $\overline{q^*}$ relationship, which is shown in Figure 19b. Similar to the $\overline{C_D^*}$ vs. S results, there are also relatively large differences between the potential flow and simulation results. The largest percent difference is about 25%, which corresponds to a flow rate of about 0.74 ($S = 0.4$). A possible reason why there are significant differences between the simulation and potential flow results is the pressure jump computed in the potential flow approach is based on an inviscid relationship, while the simulations include viscous effects. However, many of our simulation results are still quite similar to the experimental results by Graham [29] and Bearman and Trueman [30], whose results are shown in the paper by Steiros and Hultmark [25]. The forces on the porous screen are of significant interest because of their effect on the durability of the nets and mooring lines.

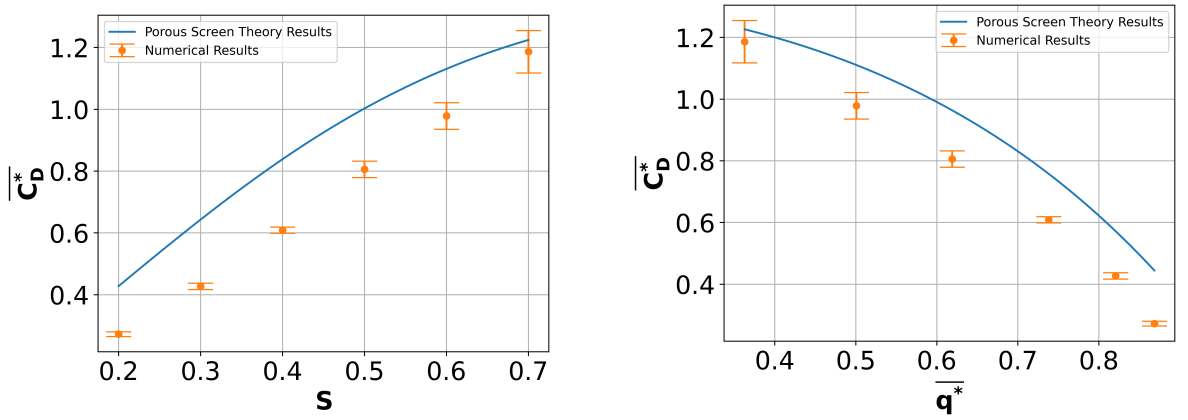

(a) Total drag coefficients results from simulations and potential flow theory as a function of the solidity

(b) Total drag coefficients results from simulations and potential flow theory as a function of the total flow rate

Figure 19

5 Conclusion/Future Work

In this thesis, we review some predominant modeling approaches that apply to the flow past an aquaculture net, and complement those results with our own investigations using high-fidelity numerical simulations of the 2D Navier-Stokes equations. Two prevalent modeling techniques for flows past nets are the panel method and the potential flow method. While the panel method provides information regarding small-scale effects and

the potential flow method provides information regarding space-averaged effects, there lacks significant research regarding a method that yields both types of information.

Using a numerical simulation approach, we provided resolved numerical simulations of the two-dimensional flow through a porous screen, formed by an array of side-by-side cylinders placed perpendicular to a free-stream flow. Based on the simulation results, we compute a variety of flow rate and force values. Our first discussion topics are regarding the sum of drag coefficients and flow rates. A main finding from the drag coefficient analysis is that the total force on the screen increases as solidity increases. Furthermore, the flow rate tends to become less harmonic as the solidity increases, which is likely related to an increased mixing of shedded vortices.

To study small-scale flow characteristics, we analyze a plot of the time-averaged flow rate through each gap for all of the cases. As the solidity increases, the flow tends to become less evenly distributed, which supports the idea that one should not assume flow past a porous screen is always uniform. Based on our results, this assumption of a uniform flow distribution is valid for solidities less than 0.4 because there is not a reasonable difference between the flow rates until $S = 0.4$. Similarly, the drag force on each cylinder tends to become less evenly distributed as the solidity increases. For example, the difference between the largest and smallest normalized drag coefficient for the drag coefficient for the $S = 0.2$ case is negligible, while the percent difference between the largest and smallest absolute value of the normalized drag coefficient for the $S = 0.7$ case is about 115%. We also study normalized time-averaged lift coefficient results for each cylinder. Two main findings are the magnitude of the normalized lift force tends to increase for cylinders farther from the center of the porous screen and there is a repulsive force between neighboring cylinders. The next discussion topic is time-averaged velocity field results. In that section we describe the effect solidity has on the velocity across the entire domain. We determine that the higher solidity porous screens have a more significant affect on the velocity field that the lower solidity screens. Similarly, the wake width tends to increase as the solidity increases. We also study velocity profiles as a function of y and x. The $\overline{u}$ vs. y velocity profiles at multiple x locations indicate fluid acceleration through the gaps, which is due to conservation of mass, however the fluid slows down before the screen due to the shielding effect. We also consider the $\overline{u}$ vs. x velocity profiles for all the cases. Some findings from the velocity profiles are the $\overline{u}$ far downstream of the porous screen for most of the cases is less than 1, and as the solidity increases, the $\overline{u}$ directly upstream and far downstream decreases.

We also compare our simulation results with results from equations derived using a potential flow method [25]. The $\overline{q^*}$ decreases as S increases for both sets of results, with the largest percent difference being less than 7%. We also analyze the square of the vertical flow rate ($\overline{v^*}^2$) results as a function of the horizontal flow rate ($q*$). The $\overline{v^*}^2$ decreases as $\overline{q^*}$ increases for both sets of results, however the percent difference between some of the numerical and potential flow results is quite significant with the largest percent difference being about 40%. We also consider the relation between $\overline{C_D^*}$ as a function of S and $\overline{C_D^*}$ as a function of $\overline{q^*}$. $\overline{C_D^*}$ is the total time-averaged drag coefficient on the screen and it is normalized by the free-stream velocity and the height of the screen. As S increased, $\overline{C_D^*}$ increased, and as $\overline{q^*}$ increased, $\overline{C_D^*}$ decreased. Also, there are some significant differences between the potential flow and simulation results with the largest percent difference being about 50% for the $\overline{C_D^*}$ vs. S analysis and about 25% for the $\overline{C_D^*}$ vs. $\overline{q^*}$ analysis. The last analysis we conduct is only considering the $\overline{u^*}$ values from the simulations as a function of S. These results inform us that the shielding effect has more of an impact on $\overline{u^*}$ for

higher solidity screens (solidity values greater than 0.5).

In this research, we conduct an initial CFD analysis of flow past porous screens with the goal of understanding small-scale and coupled fluid flow and force characteristics. We consider the following information as reasonable topics to study moving forward.

1. One could run simulations of cylinders with springs connected to the center of each cylinder. The springs would represent the strands connecting the nodes (the cylinders) together and lead to the simulation of a flexible net. One topic of interest could be the analysis of Vogel exponents. Vogel exponents are used to modify the relation between force and velocity [31]. The force on flexible structures has been determined to scale less than U^2, whereas the force on the corresponding rigid structure is larger and generally scales as U^2. The topic of Vogel exponents has been applied to a variety of topics, such as flexible beams [32], fibers [33], and leaves [34, 35]. Jin et al. experimentally determined Vogel exponents for a variety of flexible porous screens [36]. We could further this area of research by numerically determining Vogel exponents for a variety of flexible porous screens.

2. Another potential topic could be running 3D simulations. While many researchers have applied the panel method to the analysis of 3D nets [7][9][11] [37] [16][12], running full CFD simulations would provide additional insights regarding the flow-screen interactions. Some topics to consider could include how the flow is affected by the intersection of strands and how the flow rate and force results differ from the 2D analysis results.

3. Running more 2D simulations with higher Reynolds numbers would also be interesting. Higher Reynolds numbers that are greater than a critical Reynolds number will likely lead to the viscous effects to become negligible. Hoerner [38] determined that the critical Reynolds number for flow past fabric is 1000. We would want to vary both the Reynolds number based on cylinder diameter and the height of the array by running simulations with various H/D values to investigate whether this holds at lower solidities as well.

4. One could also study the pressure jump across a 2D or 3D porous screen. Zampogna and Gallaire [39] are two researchers who have conducted such an analysis. Obtaining an expression, or a set of expressions, that relate the pressure jump to many parameters, such as Re, H/D, Sn, S, and t, would contribute the development of accurate and computationally inexpensive ways to simulate flow past porous screens.

References

[1] H. Moe Føre, "Strength analysis of net structures," 01 2009.

[2] P. Klebert, P. Lader, L. Gansel, and F. Oppedal, "Hydrodynamic interactions on net panel and aquaculture fish cages: A review," *Ocean Engineering*, vol. 58, pp. 260–274, 2013. [Online]. Available: https://www.sciencedirect.com/science/article/pii/S0029801812003940

[3] H. Cheng, L. Li, K. G. Aarsæther, and M. C. Ong, "Typical hydrodynamic models for aquaculture nets: A comparative study under pure current conditions," *Aquacultural Engineering*, vol. 90, p. 102070, 2020. [Online]. Available: https://www.sciencedirect.com/science/article/pii/S014486091930216X

[4] H. Cheng, "Study on the anti-current characteristics of a new type gravity fish cage and design optimizing," Ph.D. dissertation, Ocean University of China, 2017.

[5] C.-W. Bi, Y.-P. Zhao, G.-H. Dong, T.-J. Xu, and F.-K. Gui, "Experimental investigation of the reduction in flow velocity downstream from a fishing net," *Aquacultural Engineering*, vol. 57, pp. 71–81, 2013. [Online]. Available: https://www.sciencedirect.com/science/article/pii/S0144860913000691

[6] J. Morison, J. Johnson, and S. Schaaf, "The Force Exerted by Surface Waves on Piles," *Journal of Petroleum Technology*, vol. 2, no. 05, pp. 149–154, 05 1950. [Online]. Available: https://doi.org/10.2118/950149-G

[7] I. Tsukrov, O. Eroshkin, D. Fredriksson, M. Swift, and B. Celikkol, "Finite element modeling of net panels using a consistent net element," *Ocean Engineering*, vol. 30, no. 2, pp. 251–270, 2003. [Online]. Available: https://www.sciencedirect.com/science/article/pii/S0029801802000215

[8] C.-C. Huang, H.-J. Tang, and J.-Y. Liu, "Dynamical analysis of net cage structures for marine aquaculture: Numerical simulation and model testing," *Aquacultural Engineering*, vol. 35, pp. 258–270, 10 2006.

[9] Y.-C. Li, Y.-P. Zhao, F.-K. Gui, and B. Teng, "Numerical simulation of the hydrodynamic behaviour of submerged plane nets in current," *Ocean Engineering*, vol. 33, no. 17, pp. 2352–2368, 2006. [Online]. Available: https://www.sciencedirect.com/science/article/pii/S0029801806000370

[10] H. Moe, A. Fredheim, and O. Hopperstad, "Structural analysis of aquaculture net cages in current," *Journal of Fluids and Structures*, vol. 26, no. 3, pp. 503–516, 2010. [Online]. Available: https://www.sciencedirect.com/science/article/pii/S0889974610000289

[11] C.-W. Bi, Y.-P. Zhao, G.-H. Dong, T.-J. Xu, and F.-K. Gui, "Numerical simulation of the interaction between flow and flexible nets," *Journal of Fluids and Structures*, vol. 45, pp. 180–201, 2014. [Online]. Available: https://www.sciencedirect.com/science/article/pii/S0889974613002594

[12] H. Chen and E. D. Christensen, "Development of a numerical model for fluid-structure interaction analysis of flow through and around an aquaculture net cage," *Ocean Engineering*, vol. 142, pp. 597–615, 2017. [Online]. Available: https://www.sciencedirect.com/science/article/pii/S0029801817304043

[13] T. Kristiansen and O. M. Faltinsen, "Modelling of current loads on aquaculture net cages," *Journal of Fluids and Structures*, vol. 34, pp. 218–235, 2012. [Online]. Available: https://www.sciencedirect.com/science/article/pii/S0889974612000783

[14] G. Løland, "Current forces on and flow through fish farms," Ph.D. dissertation, NTNU, 1991.

[15] H. Rudi, G. Løland, and L. Furunes, "Model Tests With Net Enclosures. Forces on and Flow Through Single Nets and Cage Systems," 1988.

[16] Y. Yao, Y. Chen, H. Zhou, and H. Yang, "Numerical modeling of current loads on a net cage considering fluid–structure interaction," *Journal of Fluids and Structures*, vol. 62, pp. 350–366, 2016. [Online]. Available: https://www.sciencedirect.com/science/article/pii/S0889974616000116

[17] P. Bore, J. Amdahl, and D. Kristiansen, "Modelling of hydrodynamic loads on aquaculture net cages by a modified morison model," 05 2017.

[18] P. C. Endresen, M. Føre, A. Fredheim, D. Kristiansen, and B. Enerhaug, "Numerical Modeling of Wake Effect on Aquaculture Nets," vol. Volume 3: Materials Technology; Ocean Space Utilization, p. V003T05A027, 06 2013. [Online]. Available: https://doi.org/10.1115/OMAE2013-11446

[19] R. Blevins, *Flow-induced Vibration*. Van Nostrand Reinhold, 1990. [Online]. Available: https://books.google.com/books?id=yJ9RAAAAMAAJ

[20] R. D. Blevins, *Applied Fluid Dynamics Handbook*. Krieger Pub., 2003. [Online]. Available: https://books.google.com/books?id=WGJDPgAACAAJ

[21] F. O'Neill, "Source models of flow through and around screens and gauzes," *Ocean Engineering*, vol. 33, no. 14, pp. 1884–1895, 2006. [Online]. Available: https://www.sciencedirect.com/science/article/pii/S0029801805002696

[22] G. Taylor, A. R. C. G. Britain), and A. R. C. Ministry of Supply, *Air Resistance of a Flat Plate of Very Porous Material*, ser. ARC technical report. H.M. Stationery Office, 1944. [Online]. Available: https://books.google.com/books?id=9B28OwAACAAJ

[23] W. D. Baines and E. G. Peterson, "An Investigation of Flow Through Screens," *Transactions of the American Society of Mechanical Engineers*, vol. 73, no. 5, pp. 467–477, 07 2022. [Online]. Available: https://doi.org/10.1115/1.4016280

[24] J.-K. Koo and D. F. James, "Fluid flow around and through a screen," *Journal of Fluid Mechanics*, vol. 60, no. 3, p. 513–538, 1973.

[25] K. Steiros and M. Hultmark, "Drag on flat plates of arbitrary porosity," *Journal of Fluid Mechanics*, vol. 853, p. R3, 2018.

[26] J. Gabbard, T. Gillis, P. Chatelain, and W. M. van Rees, "An immersed interface method for the 2d vorticity-velocity navier-stokes equations with multiple bodies," *Journal of Computational Physics*, vol. 464, p. 111339, 2022. [Online]. Available: https://www.sciencedirect.com/science/article/pii/S0021999122004016

[27] X. Ji, J. Gabbard, and W. M. van Rees, "A sharp immersed method for 2d flow-body interactions using the vorticity-velocity navier-stokes equations," *Journal of Computational Physics*, vol. 494, p. 112513, 2023. [Online]. Available: https://www.sciencedirect.com/science/article/pii/S0021999123006083

[28] G. Taylor, A. R. C. G. Britain), R. Davies, G. B. A. R. C. F. M. Panel, and A. R. C. Ministry of Supply, *The Aerodynamics of Porous Sheets*, ser. ARC technical report. H.M. Stationery Office, 1944. [Online]. Available: https://books.google.com/books?id=t_76GgAACAAJ

[29] J. M. R. Graham, "Turbulent flow past a porous plate," *Journal of Fluid Mechanics*, vol. 73, no. 3, p. 565–591, 1976.

[30] P. W. Bearman and D. M. Trueman, "An investigation of the flow around rectangular cylinders," *Aeronautical Quarterly*, vol. 23, no. 3, p. 229–237, 1972.

[31] S. Vogel, "Drag and flexibility in sessile organisms," *American Zoologist*, pp. 37–44, 1984.

[32] T. Leclercq and E. de Langre, "Drag reduction by elastic reconfiguration of non-uniform beams in non-uniform flows," *Journal of Fluids and Structures*, vol. 60, pp. 114–129, 2016. [Online]. Available: https://www.sciencedirect.com/science/article/pii/S088997461500242X

[33] X. Yang, M. Liu, and S. Peng, "Smoothed particle hydrodynamics and element bending group modeling of flexible fibers interacting with viscous fluids," *Phys. Rev. E*, vol. 90, p. 063011, Dec 2014. [Online]. Available: https://link.aps.org/doi/10.1103/PhysRevE.90.063011

[34] L. SCHOUVEILER and A. BOUDAOUD, "The rolling up of sheets in a steady flow," *Journal of Fluid Mechanics*, vol. 563, p. 71–80, 2006.

[35] S. Alben, "Self-similar bending in a flow: The axisymmetric case," *Physics of Fluids*, vol. 22, no. 8, p. 081901, 08 2010. [Online]. Available: https://doi.org/10.1063/1.3467494

[36] Y. Jin, J.-T. Kim, S. Cheng, O. Barry, and L. P. Chamorro, "On the distinct drag, reconfiguration and wake of perforated structures," *Journal of Fluid Mechanics*, vol. 890, p. A1, 2020.

[37] T. Kristiansen and O. M. Faltinsen, "Experimental and numerical study of an aquaculture net cage with floater in waves and current," *Journal of Fluids and Structures*, vol. 54, pp. 1–26, 2015. [Online]. Available: https://www.sciencedirect.com/science/article/pii/S0889974614002114

[38] S. Hoerner, "Aerodynamic properties of screens and fabrics," *Textile Research Journal*, vol. 22, no. 4, pp. 274–280, 1952. [Online]. Available: https://doi.org/10.1177/004051755202200405

[39] G. A. Zampogna and F. Gallaire, "Effective stress jump across membranes," *Journal of Fluid Mechanics*, vol. 892, p. A9, 2020.